Supplemental Information for

Seasonal differences in formation processes of oxidized organic aerosol near Houston, TX

Qili Dai[1, 2], Benjamin C. Schulze[2, 3], Xiaohui Bi[1, 2], Alexander A.T. Bui[2], Fangzhou Guo[2], Henry W. Wallace[2, 4], Nancy P. Sanchez[2], James H. Flynn[5], Barry L. Lefer[5,6], Yinchang Feng[1*], Robert J. Griffin[2, 7]

[1]State Environmental Protection Key Laboratory of Urban Ambient Air Particulate Matter Pollution Prevention and Control, College of Environmental Science and Engineering, Nankai University, Tianjin 300350, China

[2]Department of Civil and Environmental Engineering, Rice University, Houston, TX, 77005

[3]Department of Environmental Science and Engineering, California Institute of Technology, Pasaedna, CA, 91125

[4]Washington State Department of Ecology, Lacey WA, 98503

[5]Department of Earth and Atmospheric Sciences, University of Houston, Houston, TX, 77004

[6]Division of Tropospheric Composition, NASA, Washington, DC 20024

[7]Department of Chemical and Biomolecular Engineering, Rice University, Houston, TX, 77005

[*]Corresponding author: Yinchang Feng (fengyc@nankai.edu.cn)

1. Location of Measurement Site

Figure S1. Google map for the location of the measurement site (University of Houston Sugar Land, UHSL).

2. Detection limits

The detection limits for major NR-PM_1 species measured during the two campaigns were calculated as three times of the standard deviation of filter periods.

Table S1. Detection limits (DL) determined for NR-PM_1 species measured during the winter and summer campaign.

		Org.	SO_4	NO_3	NH_4	Chl
Winter	DL	0.106	0.008	0.008	0.001	0.008
	Measurement below DL	0%	0%	0%	0%	5%
Summer	DL	0.120	0.012	0.016	0.011	0.011
	Measurement below DL	0%	0%	3%	0%	50%

3. High organic nitrate mass loading periods

Figure S2 presents the scatter plots of NO_2^+ versus NO^+ for winter and summer campaigns. The slope for organic nitrate (dashed green lines, R_{ON} = 0.166) was adopted from the literature (Fry et al., 2009), the slope for inorganic nitrate (dashed blue line, R_{NH4NO3} = 0.588, 0.381 for the winter and summer campaigns, respectively) was obtained from our calibrations, and R_{obs} is the ambient NO_x^+ ratio. Most of the data observed in winter were far from the organic nitrate slope and most of the data observed in summer close to the organic nitrate slope, indicating nitrate in winter was nearly all inorganic and nitrate in summer was at least partly organic.

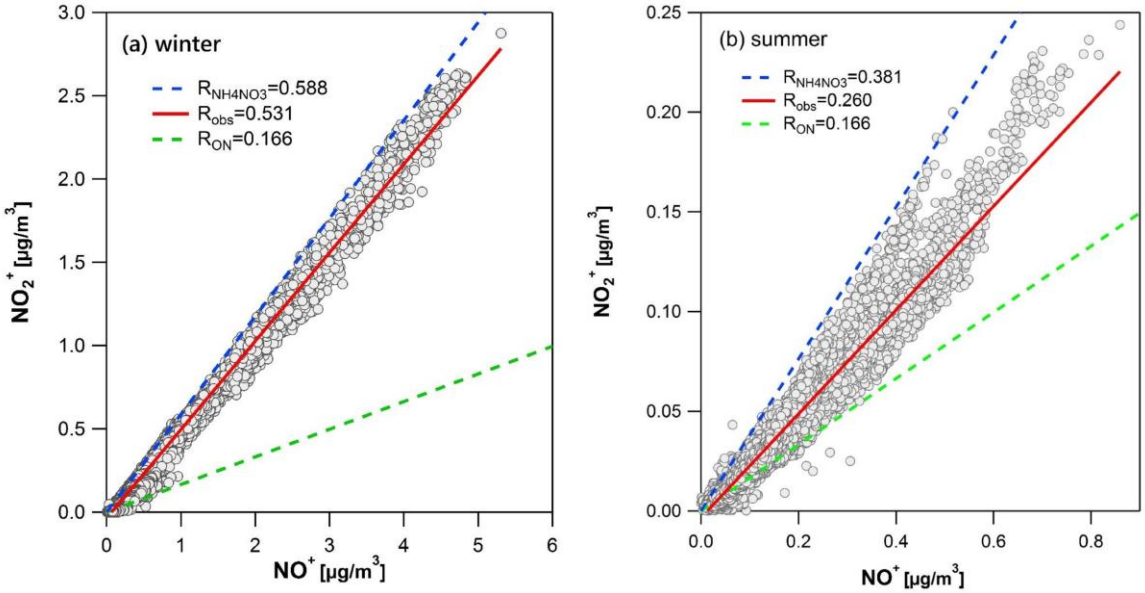

Figure S2. Scatter plots of NO_2^+ vs NO^+ for the winter and summer campaigns.

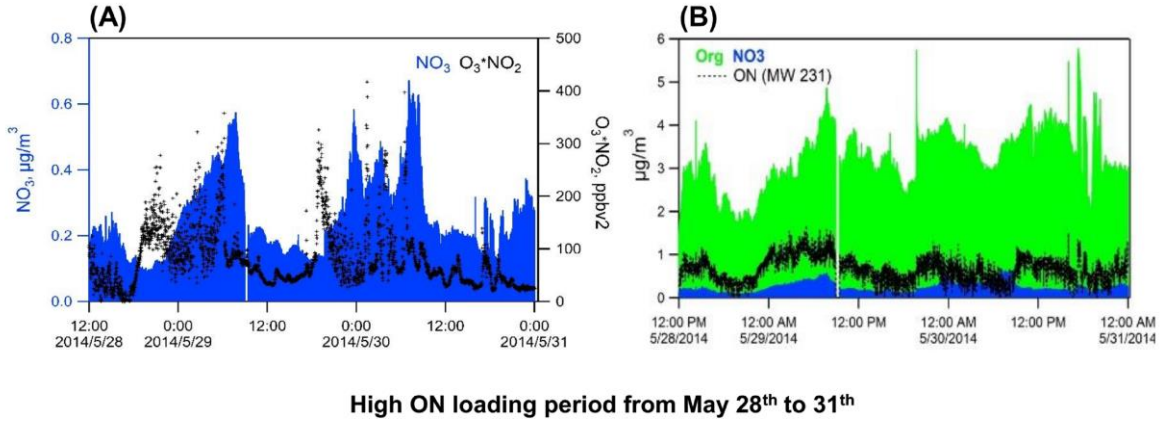

Figure S3. A high ON loading period observed during the summer campaign: (A) time series of the mass loading of NO_3 and O_3 times NO_2, (B) organics (Org), NO_3 and estimated ON.

4. PMF Analysis

4.1 Selection of PMF factor number

First, a minimum error value was applied to the error matrix, and each ion was evaluated by its signal-to-noise (SNR) ratio. Mass fragments with an average SNR between 0.2 and 2 were downweighted by increasing their errors by a factor of 2, while those mass fragments with a SNR<0.2 were removed from the dataset. Errors of the ions related to CO_2^+ (i.e., O^+, HO^+, H_2O^+, CO^+) were also downweighted to avoid excessive weighting of the signal at *m/z* 44. All isotopes were removed from the matrix given that their signals were scaled to their parent ions. The PMF2 algorithm running in robust mode with the error model set to 0 was used for PMF analysis.

The PMF solution with factor numbers greater than five and four for the winter and summer, respectively, yielded no new distinct and physical meaningful factors. The Q/Q_{exp} and the factors obtained for different FPEAK (from -1 to 1 with an increment of 0.2) values resulted in small differences in the OA components. Because of the lowest Q/Q_{exp} and because the use of FPEAK values different from zero did not improve the correlations between PMF factors and external tracers, the five- and four-factor solutions with FPEAK = 0 can be well interpreted in winter and summer, respectively. The convergence of the PMF model containing five and four factors were examined by running each model from fifteen different starting values (SEEDs 0-30 with a step value of 2). The small variation observed in Q/Q_{exp} and the mass fraction of different factors as SEED changed indicates the solutions were stable. As a result, SEED 0 was chosen for the final solution.

OA in winter

The values of Q/Q_{exp} of the PMF solution with more than three factors slightly decreased when adding a new factor into the model, indicating that the best solution probably contained at least three factors (Fig. S4). Comparing with the three-factor solution, the reconstructed OA mass with factor number great than three fitted the measured OA mass very well, and the six-factor solution had the smallest scaled residuals for ions (Fig. S5). Thus, PMF solutions containing between four and six factors could explain most of the variance of the winter dataset (Fig. S6).

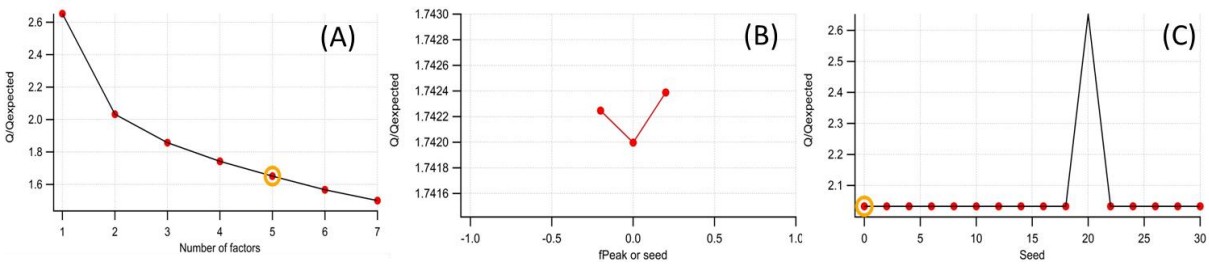

Figure S4. Q/Q_{exp} for PMF solutions containing between one to seven factors for the winter dataset (A). Q/Q_{exp} for the five-factors solution with FPEAK from -1 to 1 (B). Q/Q_{exp} for the five-factors solution with SEED from 0-30 (C).

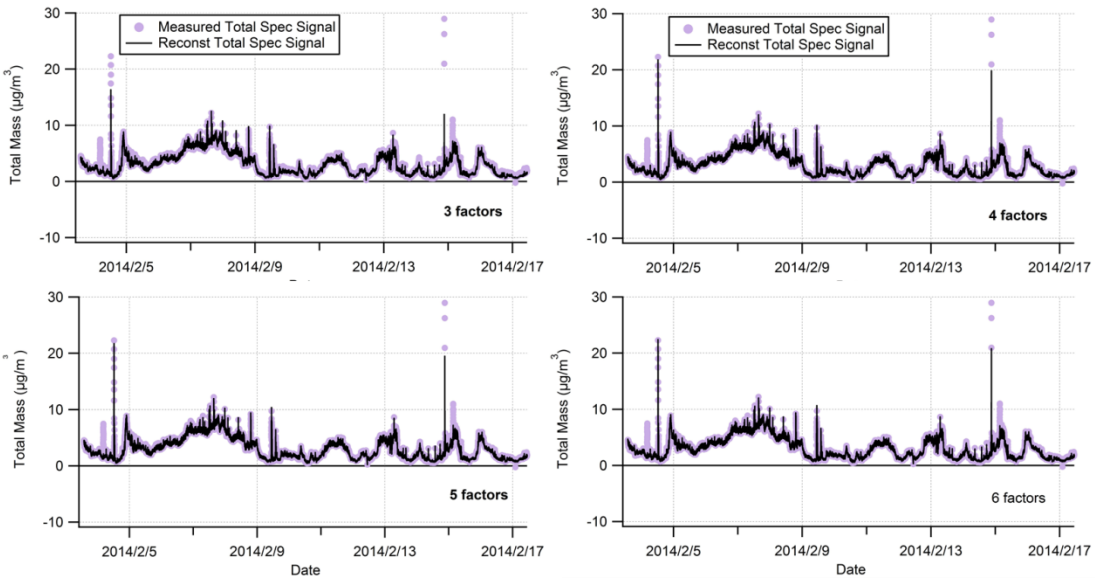

Figure S5. Measured and reconstructed submicron OA mass concentrations by PMF solutions containing three to six factors for the winter dataset.

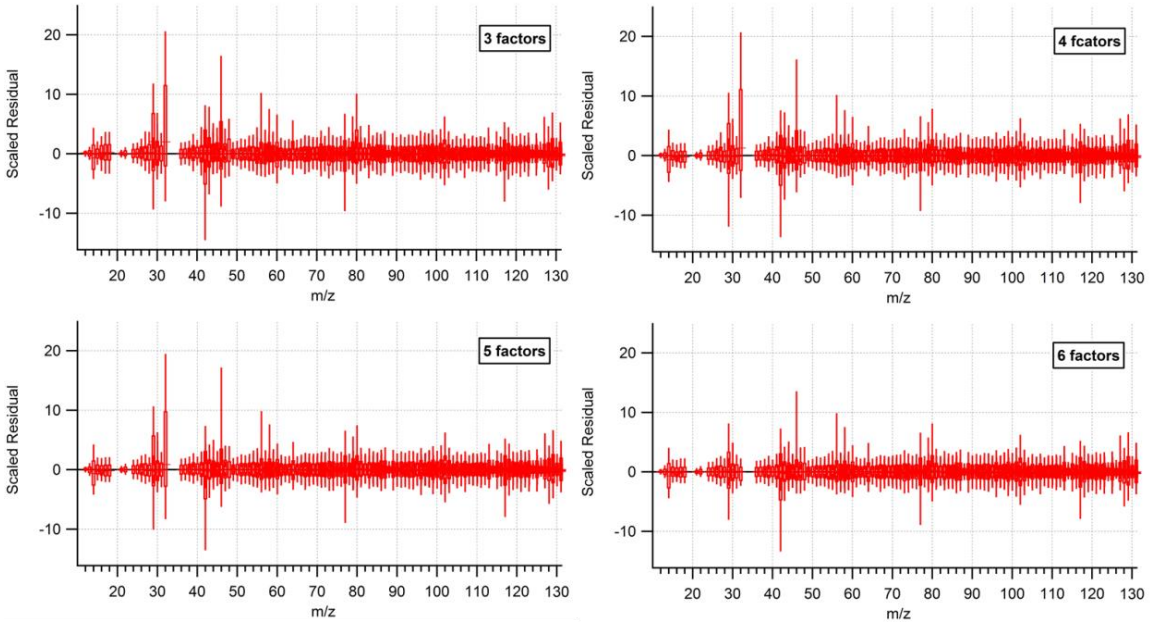

Figure S6. Scaled residuals for PMF models including three to six factors for the winter dataset.

By comparing the mass spectra of factors in the five-factor solution with that in the six-factor solution (Fig. S7), we find that F5 in the five-factor solution was split into F4 and F6 in the six-factor solution. As observed in Table S2, F4 in the six-factor solution is an unrealistic factor with both high H:C and O:C ratios, which is not physically meaningful.

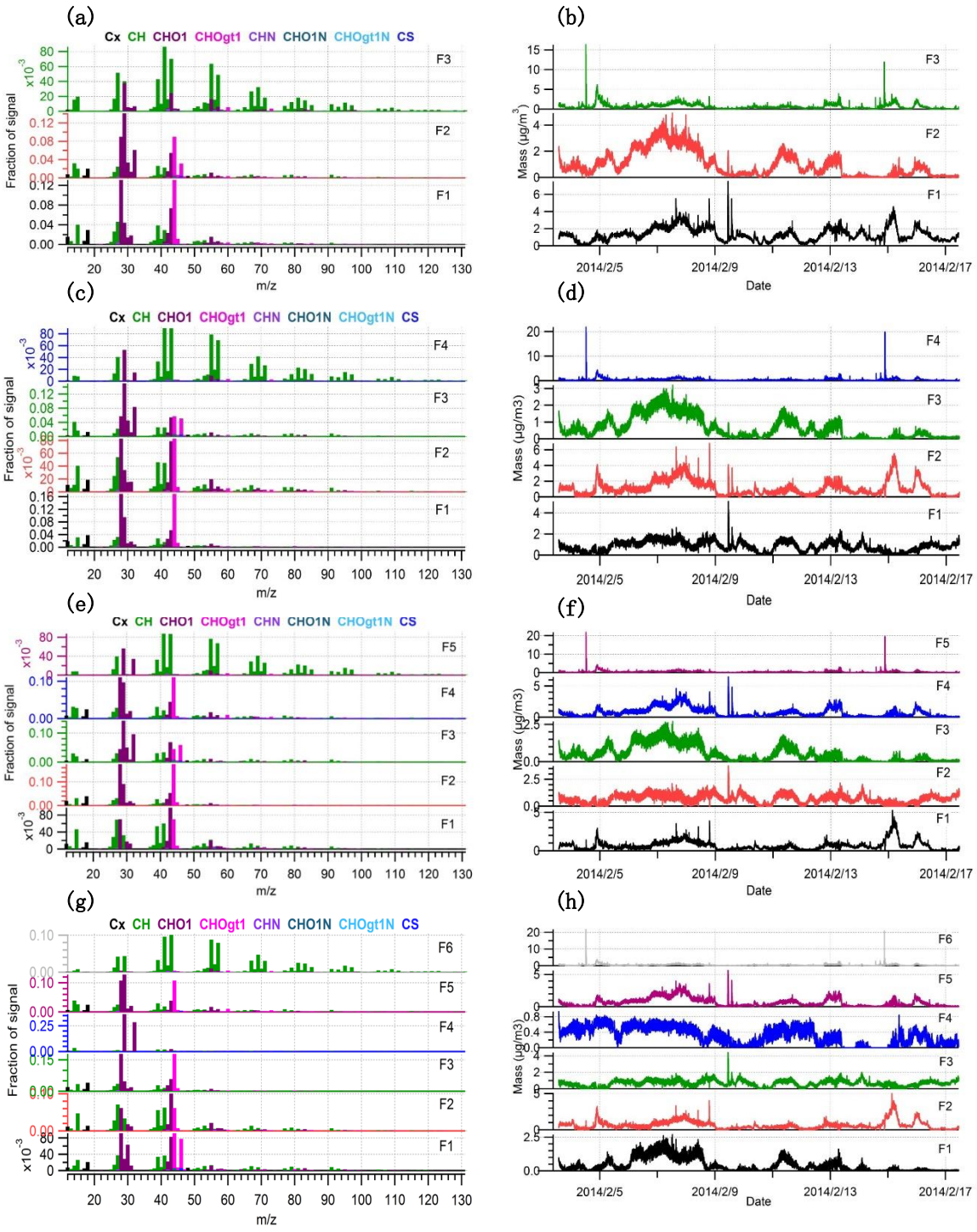

Figure S7. Comparison of mass spectra and time series for three- (a, b), four- (c, d), five- (e, f), and six- (g, h) factor PMF solutions of the winter dataset.

Table S2. H:C, O:C and OM:OC ratios of factors resulting from PMF solutions including three to six factors (F1 to F6) for the winter dataset.

	H:C/ O:C/ OM:OC					
Number of factors in PMF solution	F1	F2	F3	F4	F5	F6
3	1.52/0.72/2.10	1.84/0.99/2.49	2.03/0.11/1.33			
4	1.45/1.07/2.56	1.65/0.49/1.80	1.99/0.95/2.45	2.15/0.09/1.31		
5	**1.68/0.37/1.65**	**1.41/1.10/2.61**	**2.06/0.89/2.38**	**0.61/0.76/2.17**	**2.17/0.11/1.34**	
6	1.64/0.71/2.11	1.69/0.35/1.61	1.37/0.95/2.40	2.92/1.52/3.28	1.63/0.85/2.28	2.06/0.04/1.23

As defined in Equation S1, the spectral overlapping fraction (SOF) derived from the spectral contrast angle between factors can be used to access the degree of similarity between the mass spectra of PMF factors (Wan et al., 2002; Wallace et al., 2018). SOF varies between 0 and 1 for factors with null and complete mass spectrum overlap, respectively.

$$\mathrm{SOF} = 1 - {}^{SCA}/_{90} \quad \text{(S1)}$$

where SCA is the spectral contrast angle between PMF factors (with value of degrees).

The six-factor PMF solution exhibits higher resemblance between factors as reflected by SOFs values exceeding 0.9 for F1 and F2, as well as for F5 and F6 (Table S3). These results indicated that the optimum number of factors is likely no more than five. The PMF solutions with three to five factors have distinct chemical character as reflected by varying oxidation metrics and spectral overlapping fractions not exceeding 0.9. Although the SOF value for F1 and F3 in the five-factor solution is as high as 0.9, the oxidation states of F1 and F3 are obviously different. Because the scaled residual for ions in the five-factor solution gets smaller than those in the four-factor solution, the five-factor solution is selected as the optimum solution for the winter dataset.

Table S3 Spectral overlapping fraction (SOF) between factors in PMF solutions containing three to six factors (F1 to F6) for the winter dataset.

	F1	F2	F3	F4	F5	F6	Number of factors in PMF solution
F1	1						4
F2	0.58	1					
F3	0.82	0.68	1				
F4	0.43	0.82	0.54	1			
F1	1						5
F2	0.30	1					
F3	0.90	0.33	1				
F4	0.78	0.26	0.70	1			
F5	0.45	0.46	0.47	0.35	1		
F1	1						6
F2	1	1					
F3	0.73	0.73	1				
F4	0.66	0.66	0.76	1			
F5	0.76	0.76	0.78	0.73	1		
F6	0.73	0.73	0.76	0.70	1	1	

OA in summer

The value of Q/Q_{exp} consistently decreased when additional factors were added in the model. As shown in Fig. S8, after the four-factor solution, the incorporation of additional factors caused smaller decreases in Q/Q_{exp}, indicating that a four-factor solution could explain the variance of summer submicron OA. This is supported by Figs. S9 and S10, which indicate measured and reconstructed OA time series and the scaled residuals for each solution, respectively.

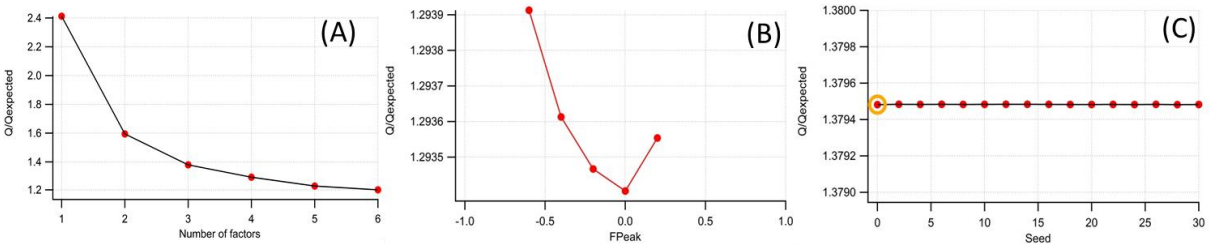

Figure S8. Q/Q_{exp} for PMF solutions containing one to five factors for the summer dataset (A). Q/Q_{exp} for the four-factors solution with FPEAK from -1 to 1 (B). Q/Q_{exp} for the four-factors solution with SEED from 0-30 (C).

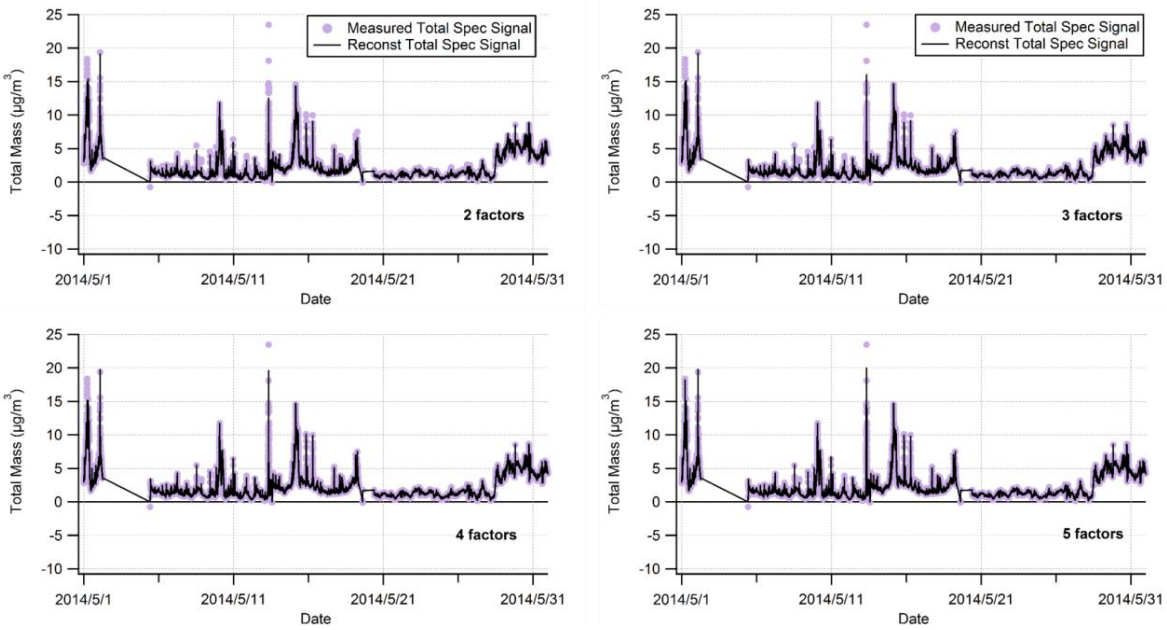

Figure S9. Measured and reconstructed submicron OA mass concentrations by PMF solutions containing two to five factors for the summer dataset.

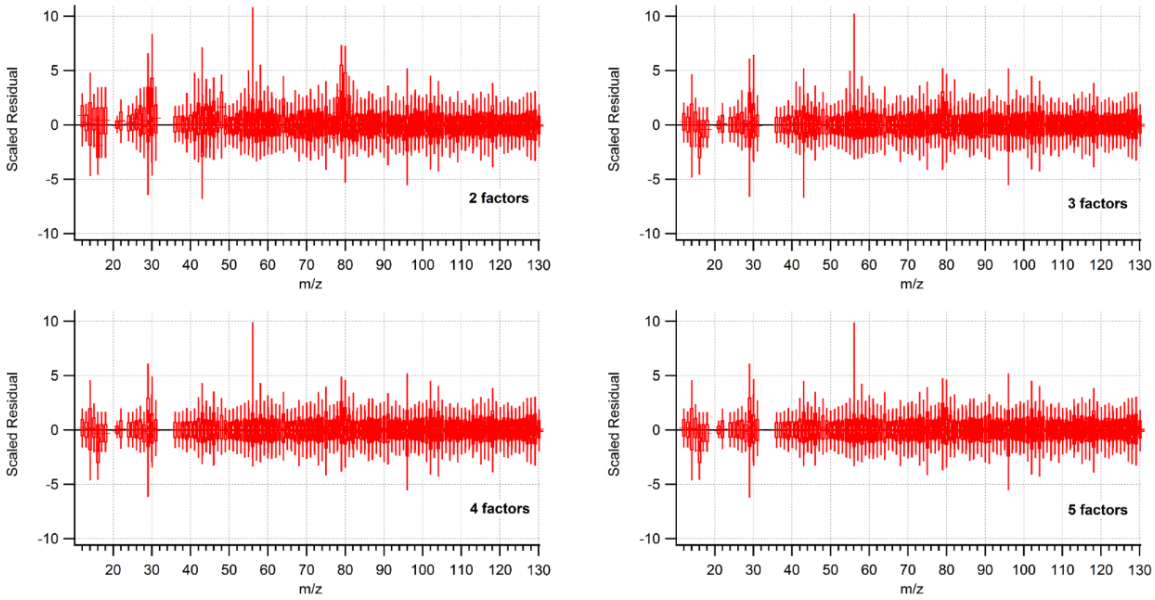

Figure S10. Scaled residuals for PMF models including two to five factors for the summer dataset.

The PMF factors associated with a five-factor solution were interpreted potentially as three POA (HOA, BBOA and COA) and two OOA (LO-OOA and MO-OOA) factors. Our spectral results (Fig. S11) show that F4 in the four-factor solution was split into F2 and F5 in the five-factor solution. In this case, F2 is unrealistic because the O/C ratio of F2 is lower than that of HOA (Table S4). In addition, there is no $C_3H_3O^+$ signal at *m/z* 55 in the mass spectra of F2, and the diel plot of F2 does not show a routine peak during local mealtime. Thus, it is unlikely to be related to cooking activities. Thus, we believe that the four-factor solution is the optimum solution for the summer dataset.

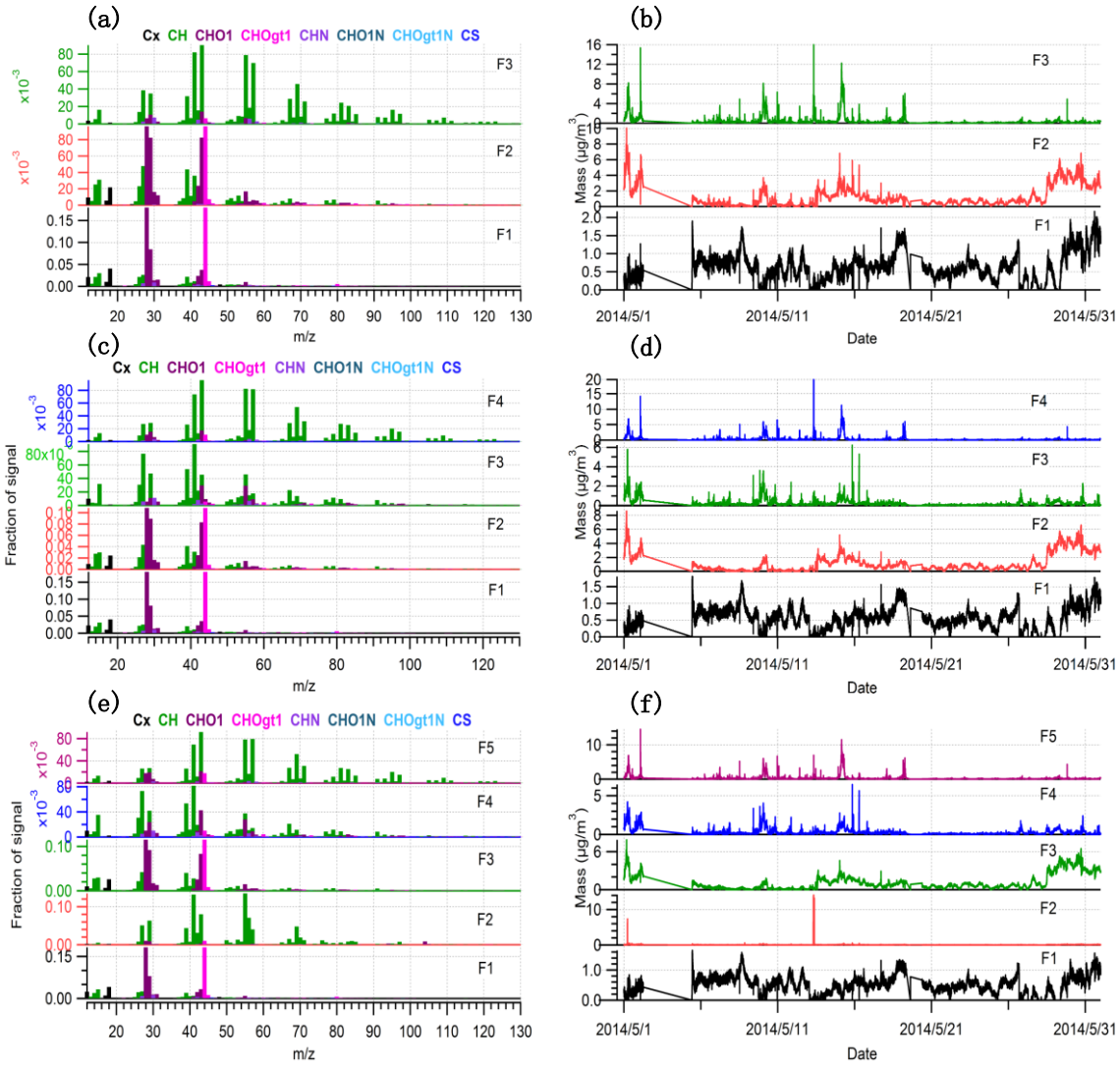

Figure S11. Comparison of mass spectra and time series for three- (a, b), four- (c, d) and five- (e, f) factor PMF solutions of the summer dataset.

Table S4. H:C, O:C and OM:OC ratios of factors resulting from PMF solutions including three to five factors (F1 to F5) for the summer dataset.

	H:C/ O:C/OM:OC				
Number of factors in PMF solution	**F1**	**F2**	**F3**	**F4**	**F5**
3	1.43/1.08/	1.66/0.66/	2.06/0.07/		
4	**1.43/1.07/2.59**	**1.63/0.74/2.12**	**1.86/0.13/1.35**	**2.09/0.07/1.28**	
5	1.42/1.08/2.61	2.03/0.05/1.24	1.61/0.78/2.18	1.85/0.17/1.41	2.08/0.10/1.32

4.2 Factor interpretation

The identified factors of OA in the winter included three POA factors (a hydrocarbon-like

OA (HOA), a biomass burning OA (BBOA), and a cooking-related OA (COA)), and two presumed SOA factors divided according to their O/C ratios (a more oxidized oxygenated OA (MO-OOA) and a less oxidized oxygenated OA (LO-OOA)). However, we were unable to identify a COA factor for the summer dataset.

Hydrocarbon-like OA (HOA)

As a common factor of OA, HOA has been identified in both winter and summer campaigns. The mass spectra of HOA is characterized by the presence of alkyl fragments, with strong signal of non-oxygenated species at *m/z* 43 ($C_3H_7^+$), *m/z* 55 ($C_4H_7^+$), *m/z* 56 ($C_4H_8^+$) and *m/z* 57 ($C_4H_9^+$) (main text, Fig. 7), which is generated during fossil fuel combustion (Lanz et al., 2008; Morgan et al., 2010; Ng et al., 2010; Wallace et al., 2018). Strong correlations were found between the time series of HOA and the $C_nH_{2n+1}^+$ and $C_nH_{2n-1}^+$ ions, e.g., $C_3H_7^+$ (r = 0.93 and 0.97 for the winter and summer dataset, respectively), $C_4H_7^+$ (r = 0.93 and 0.96), $C_4H_8^+$ (r = 0.94 and 0.92) and $C_4H_9^+$ (r = 0.90 and 0.99). The high fractions of alkyl fragments resulted in the highest H/C ratio (2.17 and 2.09 for the winter and summer) and lowest O/C ratio (0.11 and 0.07) of HOA compared to other factors. Additionally, both HOA factors in the summer and winter correlated very well with primary combustion derived trace gas species such as CO and NO (main text, Fig. 5). The HOA diurnal profiles show peaks during morning rush-hours (at 6-7:00 and 7-8:00 local time in summer and winter). Because Interstate Highway 69, with high traffic flow, is located very close to the measurement site, it is expected that traffic-related pollutants emitted from vehicle fleets would contribute to OA in both winter and summer. The decrease of HOA in the afternoon likely was due to the dilution effect of a rising PBL (Kim et al., 2017). The HOA increased from late afternoon (15:00-16:00) until the next morning, suggesting that the shallow PBL enriched air pollutants from traffic emissions. The diurnal pattern of HOA in the winter (Fig. 4, main text) was characterized with a peak during evening rush hour, indicating the enhanced association of HOA with vehicle emissions.

Biomass burning OA (BBOA)

The BBOA factor was identified using factor-tracer correlation. The commonly used tracer of biomass burning is levoglucosan ($C_6H_{10}O_5$), which has significant signal of fragment ions at

$C_2H_4O_2^+$ (*m/z* 60) and $C_3H_5O_2^+$ (*m/z* 73) (Cubison et al., 2011). These *m/z* ions have been widely used as tracers for BBOA in AMS datasets (Cubison et al., 2011; Zhang et al., 2011; Kim et al., 2017; Wallace et al., 2018). The ion signal of $C_2H_4O_2^+$ in mass spectra of BBOA is higher than that in HOA and COA for our dataset (main text, Fig. 7). Fig. 5 (main text) presents strong correlations between BBOA and $C_2H_4O_2^+$, with Pearson's *r* of 0.96 and 0.68 for the winter and summer dataset, respectively.

The mass spectra of BBOA was characterized by strong correlation with alkyl fragments ($C_nH_{2n+1}^+$ and $C_nH_{2n-1}^+$: $C_4H_8^+$ r = 0.66 and 0.77 for winter and summer, respectively) and with oxygenated ions ($C_xH_yO^+$ and $C_xH_yO_2^+$: $C_6H_{10}O^+$ r=0.75 and 0.96 for winter and summer dataset, respectively). Sources of BBOA include wood combustion for cooking and heating, waste disposal, and wildfires. BBOA corresponds to local emissions under relatively low wind speed or regional transport under relatively high wind speed. This finding is consistent with a previous study conducted in another site in Houston (Wallace et al., 2018). BBOA can gradually age during transport, leading to a broad range of O/C. The O/C ratio of BBOA is higher than that in HOA and lower than that in both OOA factors in both seasons, but the O/C of BBOA in winter (0.76) is several times of that in summer (0.13), likely indicating that BBOA in winter is from different sources and/or processed to some extent. The diurnal pattern of BBOA (Fig. 4, main text) shows overnight increases in winter, with peaks at mealtime in the morning and evening in summer. A possible reason for this difference is that wood burning during winter was used not only for cooking but also for heating, especially in the more rural northern areas of Houston, from which PM was transported. BBOA was the most abundant OA in Houston during the winter campaign, revealing the important role of residential activities in OA enhancement.

Cooking OA (COA)

COA was responsible for 22% of OA mass in winter, which is higher than HOA. However, COA was not identified during the summer campaign. The mass spectrum of COA is similar to that of HOA but exhibits more oxidized features. The O/C ratio for COA is 0.37, which is larger than that for HOA by a factor of three. Previous studies suggest that $C_3H_3O^+$ could be used as key tracer of cooking-related aerosols, as it is likely the fragment of oxygenated fatty

acids in cooking oils and animal fat (He et al., 2010; Mohr et al., 2012). The abundance of $C_3H_3O^+$ ions in *m/z* 55 in COA was higher than that in other factors (main text, Fig. 7). Moderate correlation (r= 0.65) between the time series of COA and $C_3H_3O^+$ was found. Additionally, the signals for *m/z* 55 to *m/z* 57 for COA are higher than for HOA and BBOA, which provides insight into the difference in mass spectra between COA and other POA (Zhang et al., 2011; Mohr et al., 2012). No routine peak was found during mealtimes in the diurnal pattern of COA (Fig. 4, main text).

Less-Oxygenated OOA (LO-OOA)

As a ubiquitous factor of OA, LO-OOA was identified for the two campaigns in our study. The mass spectra of LO-OOA contains less oxidized fragments as compared to MO-OOA (main text, Fig. 7). LO-OOA correlated well with CHO_{gt1} fragments in both seasons. As a proxy for fresh SOA, LO-OOA featured a low f_{44} compared to MO-OOA. The O/C ratios for LO-OOA in the winter and summer are 0.89 and 0.74, respectively, which are lower than that for MO-OOA, but higher than that for BBOA and COA. The strong correlation between LO-OOA and NO_3^- (r = 0.75 and 0.64 for winter and summer data) further confirmed its secondary nature. In addition, LO-OOA was correlated very well with ON in the summer, with Pearson's correlation coefficient of 0.73 (main text, Fig. 5). These results together confirmed the fresher nature of LO-OOA. LO-OOA accounted for 18% and 53% of OA mass in the winter and summer, respectively.

More-Oxygenated OOA (MO-OOA)

MO-OOA has a higher O:C ratio than LO-OOA. The mass spectrum of MO-OOA is comprised of the CHO^+ and CHO_{gt1} families. Fig. 5 (main text) shows strong covariance between MO-OOA and CO_2^+. In addition, MO-OOA is moderately correlated with O_3 and SO_4^{2-}, which confirms the identity of this factor. Both LO-OOA and MO-OOA have been observed in the winter and summer, indicating OOA is a ubiquitous component of OA, as reported in the literature (Ng et al., 2010). MO-OOA appears to have a notable association with regional transport as its high concentrations occurred with relatively high wind speed.

5. Effects of Photochemistry and Aqueous-phase Processing on SOA Formation

Tables S5-S8 present results of the Dunn-Bonferroni *post hoc* test for bin pairwise comparisons. The data associated with the artificially created bins in both seasons did not pass the normal test and homogeneity test of variances. The Kruskal-Wallis ANOVA for winter and summer data of the bins were significant. Thus, the Dunn-Bonferroni test was performed for the *post-hoc* pairwise comparisons. The difference between measured variables in different bins were significant if the $p' \leq 0.05$.

Table S5. Result of the Dunn-Bonferroni *post hoc* test for the pairwise comparisons of variables in different LWC bins measured in the winter campaign. Values (p') denote adjusted significance: $p' = p/n = p/15$.

	LWC ($\mu g\ m^{-3}$)	0-5	5-10	10-15	15-20	20-30
RH	20-40	<2E-16				
	40-60	<2E-16	5.80E-02			
	60-80	<2E-16	4.53E-11	1.07E-06		
	80-100	<2E-16	7.33E-08	1.33E-05	6.56E-02	
	100-120	<2E-16	6.00E-15	3.93E-11	9.89E-03	5.03E-02
WS	20-40	3.67E-15				
	40-60	4.20E-15	2.23E-02			
	60-80	8.67E-14	6.67E-02	-4.62E-02		
	80-100	7.33E-11	3.68E-02	6.66E-02	-4.93E-02	
	100-120	3.60E-15	3.60E-06	3.17E-03	7.33E-05	2.47E-02
LO-OOA	20-40	<2E-16				
	40-60	3.33E-15	9.10E-03			
	60-80	6.07E-05	2.00E-10	2.95E-04		
	80-100	6.37E-02	8.00E-10	2.13E-05	4.37E-02	
	100-120	5.73E-02	2.60E-15	4.33E-11	4.94E-04	4.73E-02
MO-OOA	20-40	3.09E-04				
	40-60	4.13E-04	6.52E-02			
	60-80	8.00E-06	3.09E-02	6.14E-02		
	80-100	9.33E-06	5.13E-03	2.02E-02	5.26E-02	
	100-120	2.27E-12	1.73E-06	9.60E-05	2.53E-03	5.52E-02

Table S6. Result of the Dunn-Bonferroni *post hoc* test for the pairwise comparisons of variables in different LWC bins measured in the summer campaign. Values (p') denote adjusted significance: $p' = p/n = p/15$.

	LWC ($\mu g\ m^{-3}$)	0-10	10-20	20-30	30-40	40-50
RH	10-20	<2E-16				
	20-30	<2E-16	1.79E-02			
	30-40	<2E-16	6.44E-02	6.43E-02		
	40-50	<2E-16	6.87E-03	6.33E-02	4.45E-02	
	50-60	<2E-16	9.33E-11	9.20E-05	2.20E-05	1.09E-02
WS	10-20	<2E-16				
	20-30	<2E-16	-3.87E-04			
	30-40	<2E-16	1.97E-03	6.67E-02		
	40-50	<2E-16	4.46E-03	6.67E-02	6.67E-02	
	50-60	<2E-16	1.13E-04	6.59E-02	6.65E-02	6.66E-02
LO-OOA	10-20	<2E-16				
	20-30	<2E-16	1.67E-07			
	30-40	<2E-16	6.67E-14	4.54E-03		
	40-50	<2E-16	3.67E-15	3.27E-05	4.48E-02	
	50-60	<2E-16	3.60E-15	4.47E-07	2.51E-02	6.67E-02
MO-OOA	10-20	5.61E-02				
	20-30	2.53E-05	1.27E-05			
	30-40	6.67E-02	6.65E-02	4.60E-03		
	40-50	1.80E-12	1.27E-12	5.17E-04	5.67E-08	
	50-60	<2E-16	<2E-16	3.47E-11	3.93E-15	1.48E-02

Table S7. Result of the Dunn-Bonferroni *post hoc* test for the pairwise comparisons of variables in different O_x bins measured in the winter campaign. Values (p') denote adjusted significance: $p' = p/n = p/15$.

	O_x (ppb)	0-10	10-20	20-30	30-40	40-50
RH	10-20	1.93E-11				
	20-30	1.27E-12	6.66E-02			
	30-40	3.73E-04	5.07E-15	<2E-16		
	40-50	3.44E-02	<2E-16	<2E-16	<2E-16	
	50-60	6.46E-02	3.73E-15	<2E-16	1.20E-12	5.34E-02
Radiometer	10-20	1.60E-10				
	20-30	1.20E-03	5.53E-15			
	30-40	3.27E-10	4.97E-02	<2E-16		
	40-50	3.07E-15	8.00E-09	<2E-16	<2E-16	
	50-60	4.33E-15	1.13E-10	<2E-16	3.33E-15	2.80E-03
LO-OOA	10-20	6.67E-02				
	20-30	4.80E-07	<2E-16			
	30-40	3.53E-08	<2E-16	1.40E-02		
	40-50	5.73E-02	4.13E-02	<2E-16	<2E-16	
	50-60	2.47E-02	8.00E-03	<2E-16	<2E-16	3.73E-02
MO-OOA	10-20	6.64E-02				
	20-30	4.20E-11	<2E-16			
	30-40	4.07E-15	<2E-16	<2E-16		
	40-50	7.33E-08	3.93E-15	1.87E-04	<2E-16	
	50-60	6.53E-14	3.80E-15	6.67E-04	4.68E-03	1.07E-06

Table S8. Result of the Dunn-Bonferroni *post hoc* test for the pairwise comparisons of variables in different O_x bins measured in the summer campaign. Values (*p´*) denote adjusted significance: *p´*=*p*/n=*p*/15.

	O_x (ppb)	0-20	20-30	30-40	40-50	50-60
RH	20-30	5.20E-15				
	30-40	<2E-16	<2E-16			
	40-50	<2E-16	<2E-16	1.20E-03		
	50-60	<2E-16	<2E-16	<2E-16	5.07E-15	
	60-70	<2E-16	<2E-16	<2E-16	<2E-16	<2E-16
Radiometer	20-30	3.40E-15				
	30-40	<2E-16	<2E-16			
	40-50	<2E-16	1.67E-15	2.20E-06		
	50-60	<2E-16	<2E-16	1.47E-03	2.53E-13	
	60-70	<2E-16	<2E-16	<2E-16	<2E-16	<2E-16
LO-OOA	20-30	2.20E-04				
	30-40	6.66E-03	3.67E-15			
	40-50	<2E-16	<2E-16	<2E-16		
	50-60	<2E-16	<2E-16	<2E-16	6.62E-02	
	60-70	<2E-16	<2E-16	<2E-16	5.33E-07	1.20E-08
MO-OOA	20-30	1.33E-11				
	30-40	2.87E-15	8.33E-05			
	40-50	4.07E-15	7.57E-04	6.67E-02		
	50-60	<2E-16	<2E-16	<2E-16	4.13E-15	
	60-70	2.73E-15	7.33E-06	4.03E-02	4.20E-02	8.00E-13

References

Cubison, M. J., Ortega, A. M., Hayes, P. L., Farmer, D. K., Day, D., Lechner, M. J., Brune, W. H., Apel, E., Diskin, G. S., Fisher, J. A., Fuelberg, H. E., Hecobian, A., Knapp, D. J., Mikoviny, T., Riemer, D., Sachse, G. W., Sessions, W., Weber, R. J., Weinheimer, A. J., Wisthaler, A., and Jimenez, J. L.: Effects of aging on organic aerosol from open biomass burning smoke in aircraft and laboratory studies, Atmos. Chem. Phys., 11, 12049-12064, https://doi.org/10.5194/acp-11-12049-2011, 2011.

Fry, J. L., Kiendler-Scharr, A., Rollins, A. W., Wooldridge, P. J., Brown, S. S., Fuchs, H., Dube, W., Mensah, A., dal Maso, M., Tillmann, R., Dorn, H. P., Brauers, T., and Cohen, R. C.: Organic nitrate and secondary organic aerosol yield from NO3 oxidation of beta-pinene evaluated using a gas-phase kinetics/aerosol partitioning model, Atmos. Chem. Phys., 9, 1431-1449, https://doi.org/10.5194/acp-9-1431-2009, 2009.

He, L. Y., Lin, Y., Huang, X. F., Guo, S., Xue, L., Su, Q., Hu, M., Luan, S. J., and Zhang, Y. H.: Characterization of high-resolution aerosol mass spectra of primary organic aerosol emissions from Chinese cooking and biomass burning, Atmos. Chem. Phys., 10, 11535-11543, https://doi.org/10.5194/acp-10-11535-2010, 2010.

Kim, H., Zhang, Q., Bae, G. N., Kim, J. Y., and Lee, S. B.: Sources and atmospheric processing of winter aerosols in Seoul, Korea: insights from real-time measurements using a high-resolution aerosol mass spectrometer, Atmos. Chem. Phys., 17, 2009-2033, https://doi.org/10.5194/acp-17-2009-2017, 2017.

Lanz, V. A., Alfarra, M. R., Baltensperger, U., Buchmann, B., Hueglin, C., Szidat, S., Wehrli, M. N., Wacker, L., Weimer, S., Caseiro, A., Puxbaum, H., Prevot, A. S. H.: Source Attribution of Submicron Organic Aerosols during Wintertime Inversions by Advanced Factor Analysis of Aerosol Mass Spectra. Environ. Sci. Tech., 42, (1), 214-220, https://doi.org/10.1021/es0707207, 2008.

Mohr, C., DeCarlo, P. F., Heringa, M. F., Chirico, R., Slowik, J. G., Richter, R., Reche, C., Alastuey, A., Querol, X., Seco, R., Peñuelas, J., Jiménez, J. L., Crippa, M., Zimmermann, R., Baltensperger, U., and Prévôt, A. S. H.: Identification and quantification of organic aerosol from cooking and other sources in Barcelona using aerosol mass spectrometer data, Atmos. Chem. Phys., 12, 1649-1665, https://doi.org/10.5194/acp-12-1649-2012, 2012.

Morgan, W. T., Allan, J. D., Bower, K. N., Highwood, E. J., Liu, D., McMeeking, G. R., Northway, M. J., Williams, P. I., Krejci, R., and Coe, H.: Airborne measurements of the spatial distribution of aerosol chemical composition across Europe and evolution of the

organic fraction, Atmos. Chem. Phys., 10, 4065-4083, https://doi.org/10.5194/acp-10-4065-2010, 2010.

Ng, N. L., Canagaratna, M. R., Zhang, Q., Jimenez, J. L., Tian, J., Ulbrich, I. M., Kroll, J. H., Docherty, K. S., Chhabra, P. S., Bahreini, R., Murphy, S. M., Seinfeld, J. H., Hildebrandt, L., Donahue, N. M., DeCarlo, P. F., Lanz, V. A., Prevot, A. S. H., Dinar, E., Rudich, Y., and Worsnop, D. R.: Organic aerosol components observed in Northern Hemispheric datasets from Aerosol Mass Spectrometry, Atmos. Chem. Phys., 10, 4625-4641, https://doi.org/10.5194/acp-10-4625-2010, 2010.

Wallace, H. W., Sanchez, N. P., Flynn, J. H., Erickson, M. H., Lefer, B. L., and Griffin, R. J.: Source apportionment of particulate matter and trace gases near a major refinery near the Houston Ship Channel, Atmos. Environ., 173, 16-29, https://doi.org/10.1016/j.atmosenv.2017.10.049, 2018.

Wan, K. X., Vidavsky, I., and Gross, M. L.: Comparing similar spectra: From similarity index to spectral contrast angle, J. Am. Soc. Mass Spectr., 13, 85-88, http://doi.org/10.1016/S1044-0305(01)00327-0, 2002.

Zhang, Q., Jimenez, J. L., Canagaratna, M. R., Ulbrich, I. M., Ng, N. L., Worsnop, D. R., and Sun, Y. L.: Understanding atmospheric organic aerosols via factor analysis of aerosol mass spectrometry: a review, Anal. Bioanal. Chem., 401, 3045-3067, https://doi.org/10.1007/s00216-011-5355-y, 2011.